

Article

Experimental and Theoretical Investigation of Rotational Behavior of Straight Mortise-Tenon Joints Considering Local Compression Perpendicular to Grain

Xingxing Liu ¹, Weidong Lu ^{1,*}, Kaifeng Liu ¹, Fengyan Xu ¹, Zhibin Ling ² and Kong Yue ¹ 

¹ College of Civil Engineering, Nanjing Tech University, Nanjing 211816, China; 201962126015@njtech.edu.cn (X.L.); liukaifeng@svolt.cn (K.L.); xfy30679@ecadi.com (F.X.); yuekong@njtech.edu.cn (K.Y.)

² School of Civil Engineering, Suzhou University of Science and Technology, Suzhou 215011, China; zbling@mail.usts.edu.cn

* Correspondence: wdlu@njtech.edu.cn

Abstract: This paper comprehensively investigates the moment-rotation relationship of straight mortise-tenon joints commonly used in Chinese antique timber buildings, focusing on analyzing the local compression mechanism at the tenon end-mortise and the tenon neck-mortise contact areas. Different compression tests were performed, and the experimental compressive stress-strain curves displayed a typical bi-linear response comprising an elastic increasing response followed by a plastic stage. The specimens subjected to middle local compression tests exhibited higher yield stress, elastic modulus, and plastic modulus than the others. Cyclic loading tests were conducted on twelve mortise-tenon joints with varying lengths, widths, and heights of the tenon to investigate the rotational behavior of the joints under alternating loading directions. The hysteresis curves of the tested specimens generally showed a “Z” shaped pinching effect, indicating limited energy dissipation of the joints during cyclic loading. The length and width of the tenon were observed to have a significant influence on the joint rotational behavior. Finally, a theoretical model was proposed to predict the moment-rotation relationship of the mortise-tenon joint, considering the proposed bilinear stress-strain relationship for wood under compression perpendicular to the grain. The predicted results obtained by the proposed theoretical model were generally validated by the experimental results.

Keywords: timber structure; straight mortise-tenon joints; local compression; moment-rotation relationship; cyclic loading test



Citation: Liu, X.; Lu, W.; Liu, K.; Xu, F.; Ling, Z.; Yue, K. Experimental and Theoretical Investigation of Rotational Behavior of Straight Mortise-Tenon Joints Considering Local Compression Perpendicular to Grain. *Buildings* **2023**, *13*, 1839. <https://doi.org/10.3390/buildings13071839>

Academic Editor: Nerio Tullini

Received: 1 June 2023

Revised: 3 July 2023

Accepted: 18 July 2023

Published: 20 July 2023



Copyright: © 2023 by the authors. Licensee MDPI, Basel, Switzerland. This article is an open access article distributed under the terms and conditions of the Creative Commons Attribution (CC BY) license (<https://creativecommons.org/licenses/by/4.0/>).

1. Introduction

A characteristic of the Chinese architectural culture is traditional timber structures. Many antiqued timber structures (Figure 1) have risen in recent years due to the promotion of traditional culture and the popularization of historical inheritances. Generally, the ancient Chinese timber structures were built according to traditional construction technology, dating back to the Song and Qing dynasties [1,2]. The Chinese traditional construction technology is an experience-based construction method. The dimensions of components and connections are more determined by geographical location than by structural demands.

In contrast, the construction of antique timber structures needs to conform to the design concepts of modern engineering structures, which requires accurate calculation and assessment of the structural performance of components, joints, and the whole system. It is well-known that the mortise-tenon joint is a typical semi-rigid joint in traditional timber structures, and the semi-rigid mechanical behavior of the joint is generally simulated by spring elements in the structural analysis of the overall structure [3–5]. However, a theoretical method for predicting the semi-rigid behavior of the mortise-tenon joints is still

immature, and the input values for the parameters of the spring elements were usually obtained by experiments. Therefore, it is essential to have further study and develop an effective theoretical moment-rotation model for the joints.



Figure 1. Antique timber building in Nanjing.

Among the various types of mortise-tenon joints, the straight type is widely used (Figure 2). When the joint is under loading, the tenon rotates in the mortise and the mechanical behavior of the joint is mainly determined by the compression and the friction between the tenon and the mortise. During the joint rotation, the compression area (Figure 3) formed by the extrusion is decided by the width and length of the tenon and varies with the length of the tenon in the mortise during the tenon pull-out. And the friction will take effect when the tenon fits tightly with the mortise (Figure 3) during rotation.



Figure 2. Straight mortise-tenon in timber frame.

Several researchers have experimentally investigated the failure patterns and mechanical behavior of the mortise and tenon joints. Xie et al. [6–8] conducted a series of surface topography and hardness tests to determine the critical parameters of the constitutive model for the friction behavior between mortise and tenon. Guan et al. [9,10] experimentally studied the mortise-tenon joints with different intercalation degrees and analyzed the joint contact stress and strain using finite element modelling. Xu et al. [11] performed a mechanical analysis to establish the mechanical models of straight mortise-tenon joints. Chen et al. [12] performed low-cyclic loading tests of 23 groups of one-way straight mortise-tenon joints to obtain $M-\theta$ skeleton curves, stiffness degradation, and equivalent viscous damping of the joints. Lydia et al. [13] developed an experimental investigation of the behavior of traditional timber mortise-tenon T-joints under monotonic and cyclic loading. Besides experiments, theoretical works were also conducted to build theoretical moment relationships considering gap, coefficient of friction, etc. Keita et al. [14]

analyzed the mechanical performance of mortise-tenon joints with a gap and established a theoretical equation to define the relationship between the bending moment and rotation. Yang et al. [15,16] evaluated the influence of the gap on the performance of mortise-tenon joints and deduced a formula for calculating the joint stiffness. Ma et al. [17] studied the influence of clearance, coefficient of friction, and wood material on the performance of mortise-tenon joints. Zhang et al. [18] investigated the effect of gaps on the rotational behavior of straight mortise-tenon joints. He et al. [19] proposed a theoretical model of the bending moment for a loose mortise-tenon joint. Previous research on mortise-tenon joints mainly focuses on the influence of the coefficient of friction and the gap between mortise and tenon. Theoretical models for the rotation of the joint were also proposed. However, there has been limited research on the influence of different compressive patterns perpendicular to the grain of the tenon on the performance of the mortise-tenon joint.

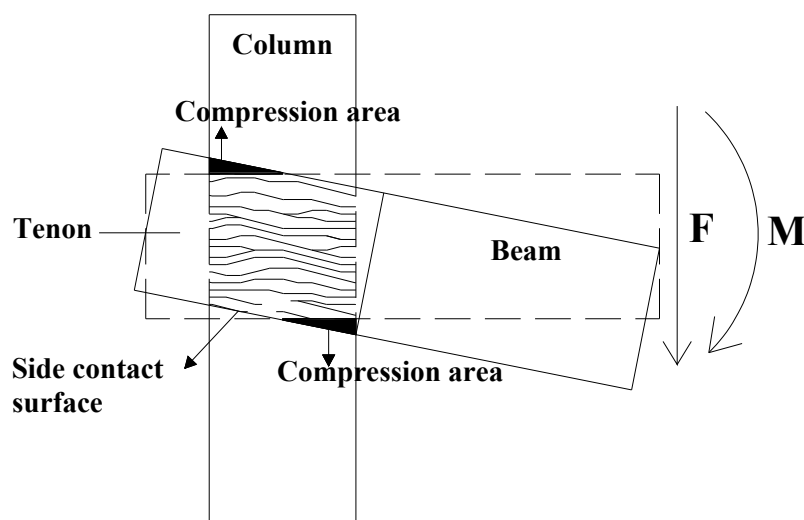


Figure 3. The mechanical model of the mortise-tenon joint.

This study used compression perpendicular to grain tests in different compression patterns to obtain the constitutive model for wood perpendicular to the grain. Then, cyclic loading tests of twelve straight mortise-tenon joints were performed to investigate the failure patterns and behavior of the joint. According to the analysis of the mechanical behavior of the joint, a theoretical model of the moment-rotation relationship considering the local compression effect was proposed to predict the rotational behavior of the mortise-tenon joint and validated by experimental results.

2. Compression Tests Perpendicular to Grain

The compression patterns of tenon perpendicular to the grain can be generally classified into three types: middle local compression, end local compression, and full compression. Local compression perpendicular to the grain leads to higher compressive strength than full compression perpendicular to the grain, as the wood fibers outside the pressure surface also contribute to compressive force sharing [20–23]. In the rotation of the mortise-tenon joint, the end of the tenon is, in the end, local compression perpendicular to the grain, and the neck of the tenon is in the middle local compression perpendicular to the grain. There probably be some difference between the stress and strain of the above-mentioned two kinds of local compression patterns. As a result, it is necessary to conduct local compression tests perpendicular to the grain to gain the constitutive relationship. This will provide a basis for further theoretical derivation of the mechanical properties of mortise-tenon joints.

2.1. Materials

The timber used in this study was Chinese fir, having an average moisture content of 14.2% and an average density of 510 kg/m³. Chinese fir was selected due to its wide applications in antique timber structures. The mechanical properties of the wood obtained according to timber material testing standards [24–27] are listed in Table 1.

Table 1. Mechanical parameters of wood.

Properties	Values (MPa)
Elastic modulus parallel to grain E_p	6400
Compressive strength parallel to grain f_c	35.3
Tensile strength parallel to grain f_t	67.2
Shear strength parallel to grain f_v	5.6

2.2. Test Setup

To obtain the compressive stress-strain relationship perpendicular to grain at different locations of the tenon, three kinds of local compression tests (middle, end and full) perpendicular to grain were carried out according to the Chinese National Standard GB/T 50329-2012 [28]. The details of the samples are shown in Table 2. All the samples were made of the same batch of wood used for the mortise-tenon joints. Figure 4 shows the test setup. The load was applied by a hydraulic servo test machine with a capacity of 60 tons at a loading rate of 1 mm/min and recorded by a 5-ton load sensor. Two linear variable displacement transducers (LVDT) were symmetrically set at the two plates welded to the loading steel plate to measure compression deformation, as shown in Figure 4.

Table 2. Details of samples.

Sample Group Code	Compression Pattern	Length/mm	Width/mm	Height/mm	Number of Replicates
JY-H	Middle local compression	240	80	80	5
DJY-H	End local compression	240	80	80	5
QY-H	Full compression	120	80	80	5

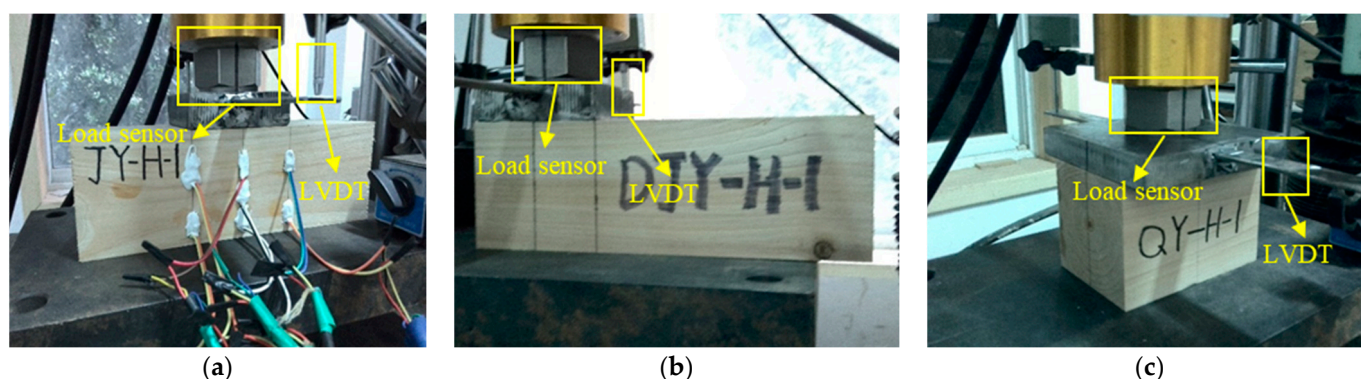


Figure 4. Compression perpendicular to the grain. (a) middle local compression, (b) end local compression, (c) full compression.

2.3. Experimental Results

Figures 5–7 show the typical failure modes of the tested specimens. It can be seen from Figures 5 and 6 that both the JY-H and the DJY-H samples exhibited serious failure of wood fiber and splitting perpendicular to the grain. In the process of loading, the pressure face under the loading plate showed concave deformation, then, the surface outside of the

pressure area showed extrusion deformation with the growth of concave deformation due to the connection of wood fiber, and the inverted triangle embedment-pressure area was formed near the edge of pressure face (Figures 5a and 6a). At the end of the sample, far away from the pressure area, the splitting failure perpendicular to the grain of wood fibers was observed due to the tensile stress perpendicular to the grain, as shown in Figures 5b and 6b. QY-H samples exhibited the crush in the middle of the sample and splitting perpendicular to the grain in the middle of the side surface, as shown in Figure 7.

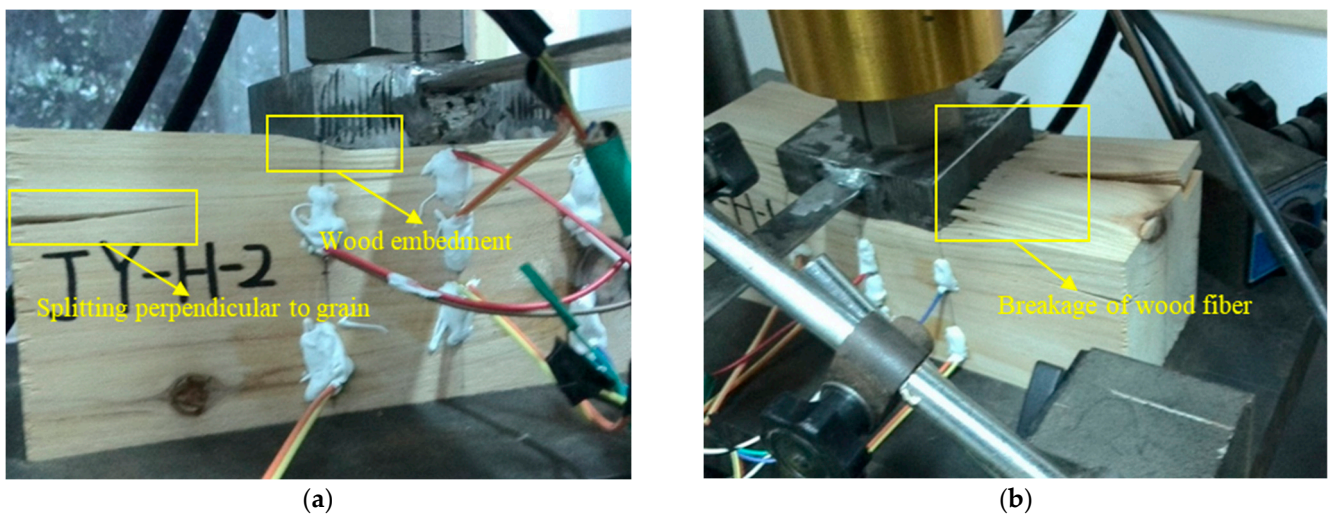


Figure 5. Failure patterns of JY-H samples. (a) concave deformation of the sample, (b) breakage of wood fiber.

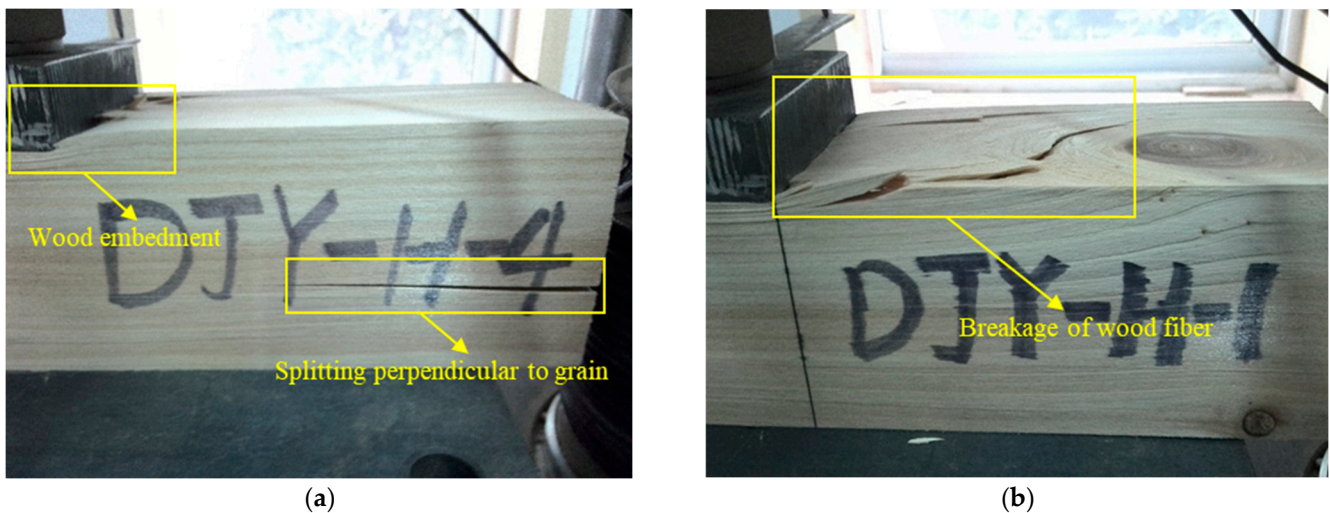


Figure 6. Failure patterns of DJY-H samples. (a) concave deformation of the sample, (b) breakage of wood fiber.

Figure 8a–c depicts the local stress-strain relationship curves obtained by the compression tests, and the average curves are shown in Figure 8d. It is observed from Figure 8d that the curves exhibited a typical bi-linear response of the elastic and plastic stage, which is characterized by an initial increasing response followed by an obvious yield plateau to failure indicating good ductility. In the elastic stage, the average curves of the three groups almost coincide at the beginning and then begin to separate at a strain of 0.005, indicating a significant difference in elastic modulus. In the plastic stage, the stress of JY-H and DJY-H samples exhibits a hardening trend, while the stress of the QY-H sample keeps a near horizontal growth trend.

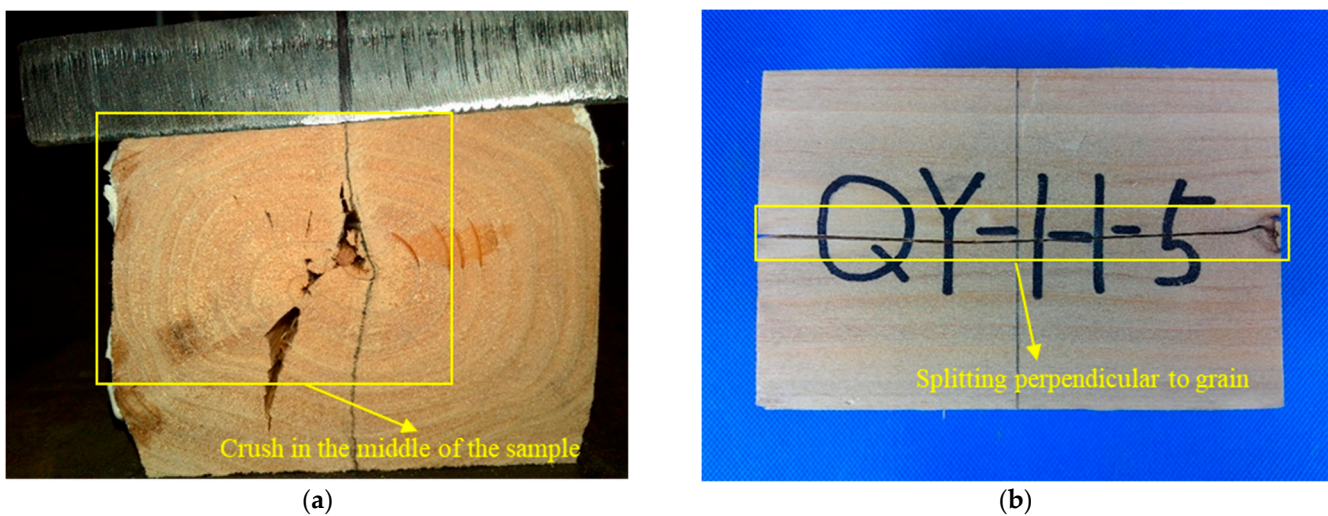


Figure 7. Failure patterns of QY-H samples. (a) crush deformation of the sample, (b) splitting perpendicular to grain.

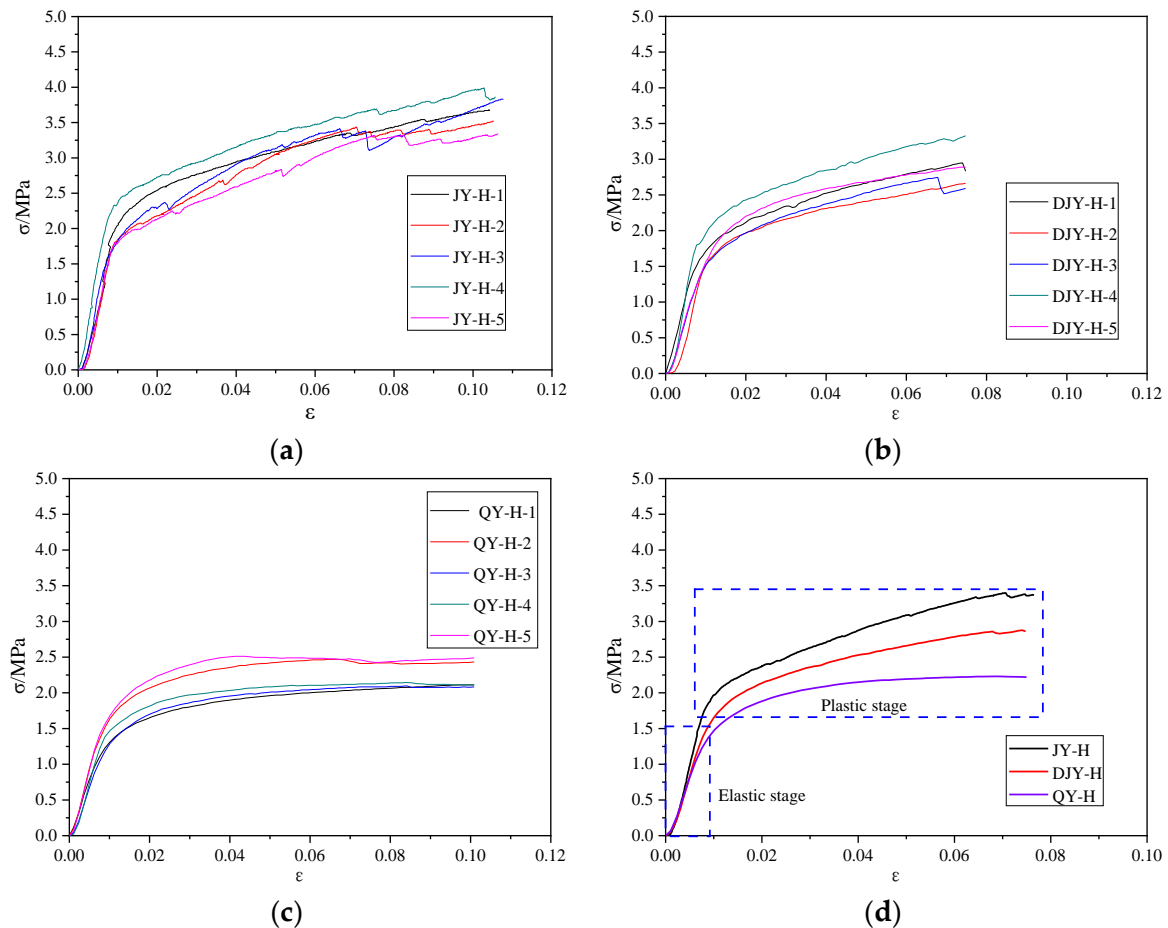


Figure 8. Stress-strain curve of three groups of samples. (a) group JY-H, (b) group DJY-H, (c) group QY-H, (d) average curves of three groups of samples.

2.4. Constitutive Model for Wood Perpendicular to Grain

To simplify the experimental stress-strain relationships, a bi-linear model was used to characterize the constitutive model for wood perpendicular to the grain. Several methods have been proposed to estimate the yield point of the curves without an obvious yield point [29–32]. The standard GB/T 50329-2012 [28] and ISO 13061-5 [33] reported that the

yield point A, as shown in Figure 9a, is determined from the diagram of compression perpendicular to grain as the ordinate of the point where the tangent of the angle formed by the tangent to the curve with the stress axis is 50% greater than its value in the linear portion of the diagram. In the standard BS EN 408-2010 [34], the yield point A is defined by the intersection of a line parallel to the linear elastic part of the strain-stress curve, offset by 1% of the specimen strain, as shown in Figure 9b. In the methods above, it can be found that the actual yield point A does not coincide with the yield point B of the simplified bi-linear curve, which causes the yield strain of the bi-linear curve to be smaller than the actual yield strain.

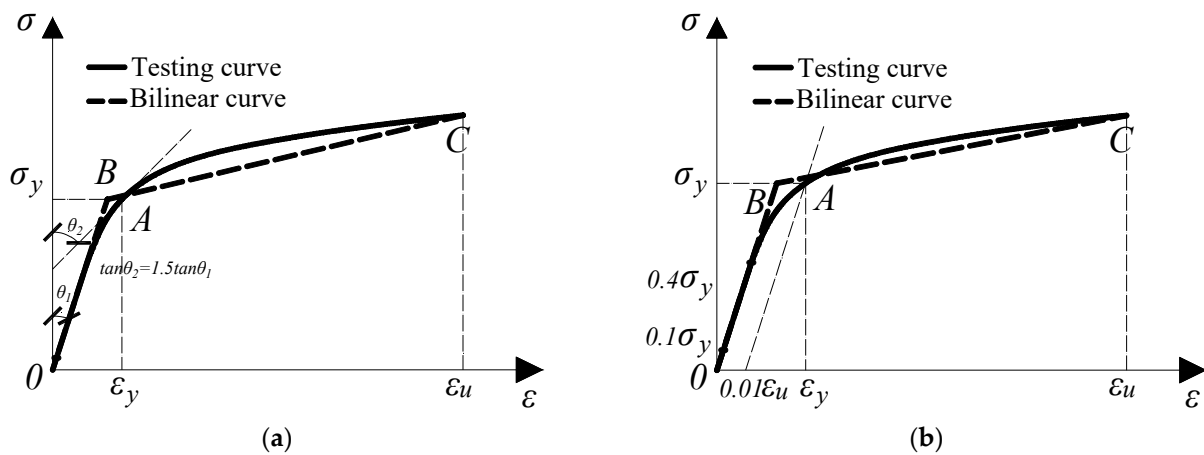


Figure 9. Methods used for the estimation of the yield point. (a) method of ISO 13061-5 and GB/T 50329, (b) method of BS EN 408.

This paper used a “most approximate area” method to estimate the yield point of the strain-stress curves, as shown in Figure 10. The basic principle of this method is that the energy area under the bi-linear curve is the most approximate to the area under the real experimental strain–stress curve. The advantage of this method is that the estimated yield point is in the real strain-stress curve. According to the most approximate area method, the elastic modulus perpendicular to grain E_{ec} is defined as the gradient of the straight line from original point O to yield point A, the plastic modulus perpendicular to grain E_{pc} is obtained by calculating the secant stiffness from the yield point A to the ultimate point B. The bilinear model can be expressed by Equation (1), which lists the relative mechanical properties in Table 3. It is observed that the yield stress of the JY-H group is 14.0% and 32.4% higher than that of the DJY-H and QY-H groups, respectively. The elastic modulus of the JY-H group is 25.1% and 36.5% higher than that of the DJY-H and QY-H groups, respectively. The plastic modulus of the JY-H group is 27.1% and 97.7% higher than that of the DJY-H and QY-H groups, respectively. Generally, it is found that the specimens that experienced the middle local compression test exhibited the highest yield stress, elastic modulus and plastic modulus compared to the other specimens.

$$\sigma = \begin{cases} E_{ec}\epsilon & 0 < \epsilon \leq \epsilon_y \\ E_{ec}\epsilon_y + E_{pc}(\epsilon - \epsilon_y) & \epsilon > \epsilon_y \end{cases} \quad (1)$$

Table 3. Average mechanical properties of the samples.

Group of Samples	Yield Stress σ_y (MPa)	Yield Strain ϵ_y	Elastic Modulus Perpendicular to Grain E_{ec} (MPa)	Plastic Modulus Perpendicular to Grain E_{pc} (MPa)
JY-H	1.96	0.010	199.3	25.3
DJY-H	1.72	0.011	159.3	19.9
QY-H	1.48	0.010	146.0	12.8

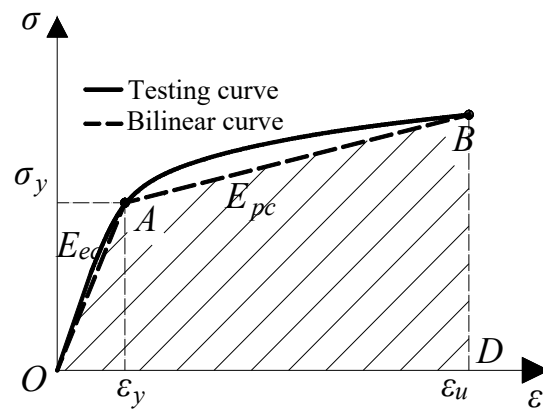


Figure 10. A “most approximate area method” for the bi-linear model.

3. Cyclic Loading Tests

The straight mortise-tenon joint is a typical semi-rigid joint in a traditional timber structure and rotates obviously under lateral load. To study the rotational behavior of the mortise-tenon joints, cyclic loading tests were carried out to obtain the mechanical behavior of the joints in alternating loading directions.

3.1. Testing Specimens

According to traditional timber construction technology, twelve T-shaped straight mortise-tenon joints, as shown in Figure 11, were designed to experience cyclic loading tests. Table 4 summarizes the test matrix and details of the specimens in this study. The experimental variables mainly include the tenon’s length, width, and height. The length direction of the tenon corresponds to the longitudinal direction of the wood grain, while the height and width directions of the tenon align with the transverse direction of the wood grain. Specimen L170 (length)-W50 (width)-H140 (height), regarded as a controlled specimen, is the mortise-through-tenon joint with a tenon length equal to the diameter of the column. The height and width are equal to the beam height and 1/3 width of the beam, respectively [35]. Specimen L128-W50-H140 was fabricated with a 128 mm tenon length to investigate the influence of the tenon length (L). Specimens L170-W40-H140 and L170-W50-H120, with the width and height of 40 mm and 120 mm, respectively, were used to investigate the influence of the tenon width (W) and tenon height (H).

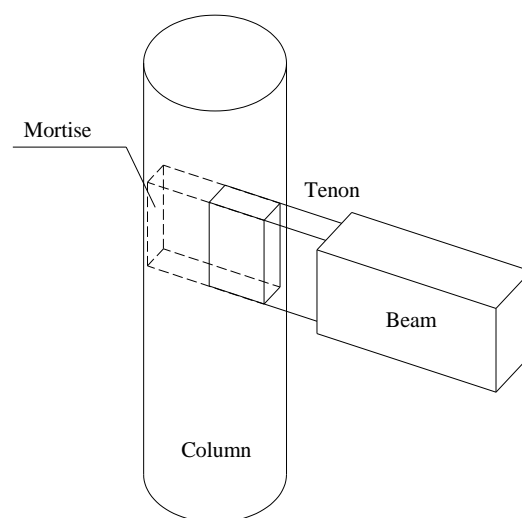


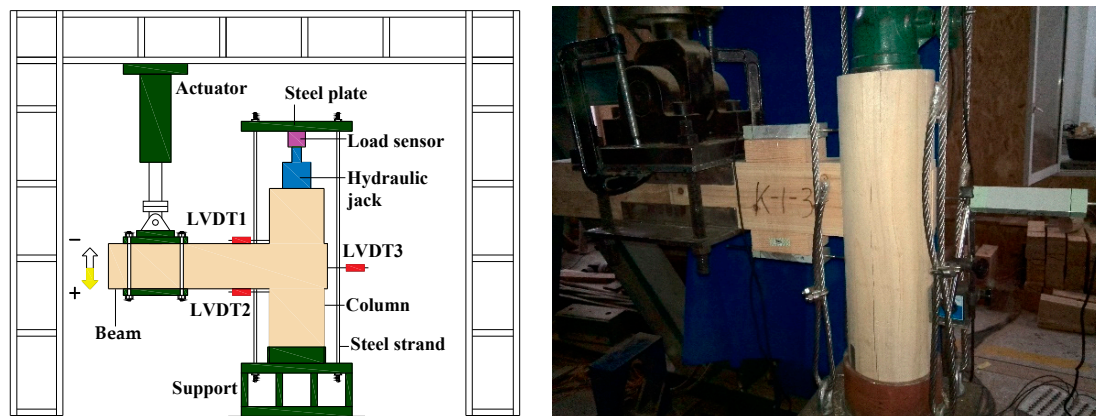
Figure 11. The mortise-tenon model.

Table 4. Details of specimens.

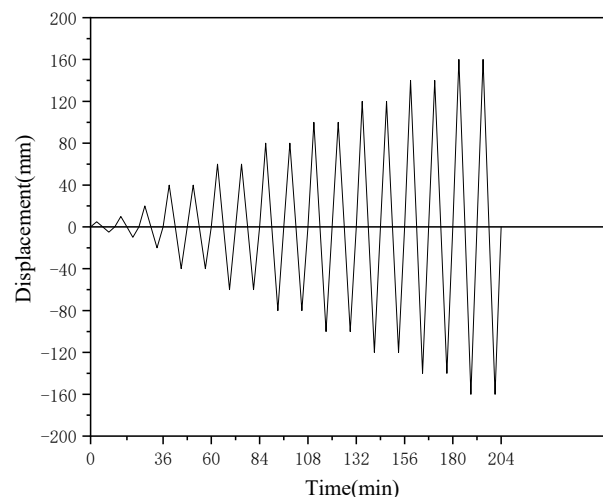
Specimen Code	Dimensions of the Tenon (mm)			Number of Replicates
	<i>L</i>	<i>W</i>	<i>H</i>	
L170-W50-H140	170	50	140	3
L128-W50-H140	128	50	140	3
L170-W40-H140	170	40	140	3
L170-W50-H120	170	50	120	3

3.2. Test Setup and Loading Protocol

The test setup for cyclic loading tests is shown in Figure 12. The column was placed at a steel boot. To simulate a real situation, A axial force of 10 kN was applied to the column by a hydraulic jack. Two LVDTs (LVDT1 and LVDT 2) were placed on both the top and bottom of the beam near the joint area to record the relative displacement and to calculate the rotation angle of the joint. Moreover, LVDT 3 was set at the end of the tenon to measure the pull-out displacement of the tenon. The cyclic load was applied at the end of the beam by a hydraulic servo actuator, as shown in Figure 12.

**Figure 12.** Schematic representation (left) and actual photograph (right) of the test setup.

The loading protocol is shown in Figure 13. First, a single loading cycle was performed at displacement amplitudes of 5, 10 and 20 mm, followed by two additional loading cycles at 40, 60, 80, 100, 120, 140 and 160 mm. The test was terminated when the load dropped below 85% of the ultimate load, or the specimen was severely damaged.

**Figure 13.** Loading protocol.

3.3. Typical Failure Modes

Figure 14 illustrates the typical failure modes of the specimens that experienced cyclic loading tests. At the loading amplitude of 20 mm, no obvious damage was observed for all the tested specimens, but squeaky sounds were heard during testing due to squeezing and slipping between the mortise and tenon. As the loading displacement increased to 60–80 mm, the tenon was gradually pulled out (Figure 14a), and a partial fracture of wood fiber in the tenon at the contact area was observed in Figure 14b. When the loading displacement reached 120–160 mm, the end of the tenon cracked transversally due to extrusion (Figure 14c), and the load dropped dramatically.

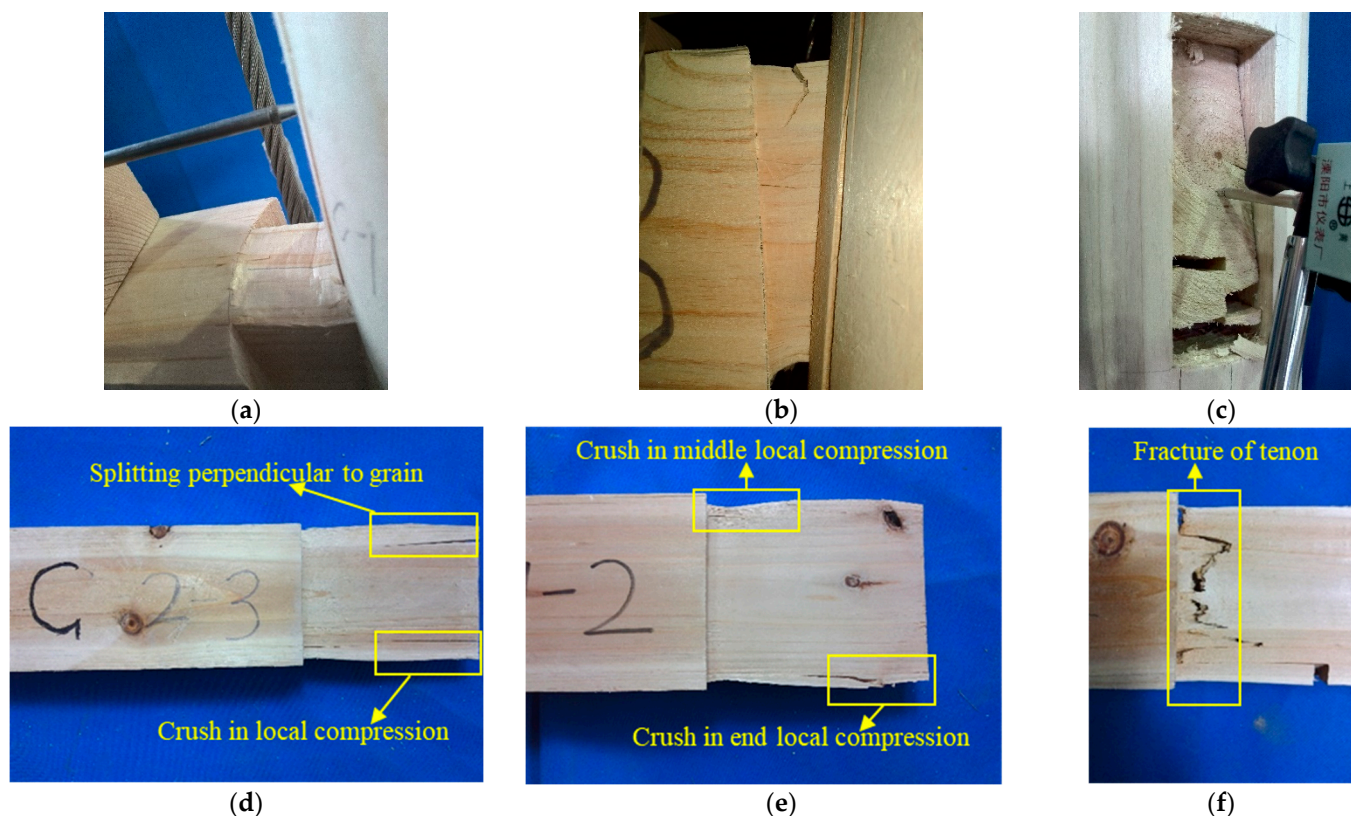


Figure 14. Failure patterns observed in the specimens: (a) Tenon pull-out; (b) Compression crush at the neck of the tenon; (c) Crack at the end of tenon; (d) Crush in local compression; (e) Split perpendicular to grain; (f) Fracture of the neck of the tenon.

The failure patterns of the specimens can be categorized into three primary types: (1) Tenon pull-out, observed in all specimens during the loading process. The tenon pullout amount of specimens L 128-W50-H140 was larger than that of the specimens with 170 mm tenon length, which indicates that the initial length of the tenon in mortise may affect the pull-out amount during rotation. (2) Crush in local compression, observed at the neck and end of the tenon, as depicted in Figure 14d,e. The shape of the compressive area at the neck of the tenon is an inverted triangle, and the shape of the compressive area at the end of the tenon is a right-angled triangle. (3) Fracture of tenon, which was only observed in specimen L170-W50-H120, as shown in Figure 14f.

3.4. Hysteresis Curves

Figure 15 indicates that the hysteresis curves of the tested specimens generally exhibit a “Z” shape indicating a typical pinching effect. The slope of the unloading curve was close to zero, and the load dropped rapidly in each hysteresis loop. These phenomena suggest that the anti-rotation ability of the joint decreased gradually due to the plastic deformation

in the loading phase, as evidenced by the near-horizontal loading force in the unloading phase. As the displacement amplitude increased, the peak value of the bending moment tended to be flat, but the hysteresis loop area increased, and the energy dissipation of the mortise-tenon joint also increased.

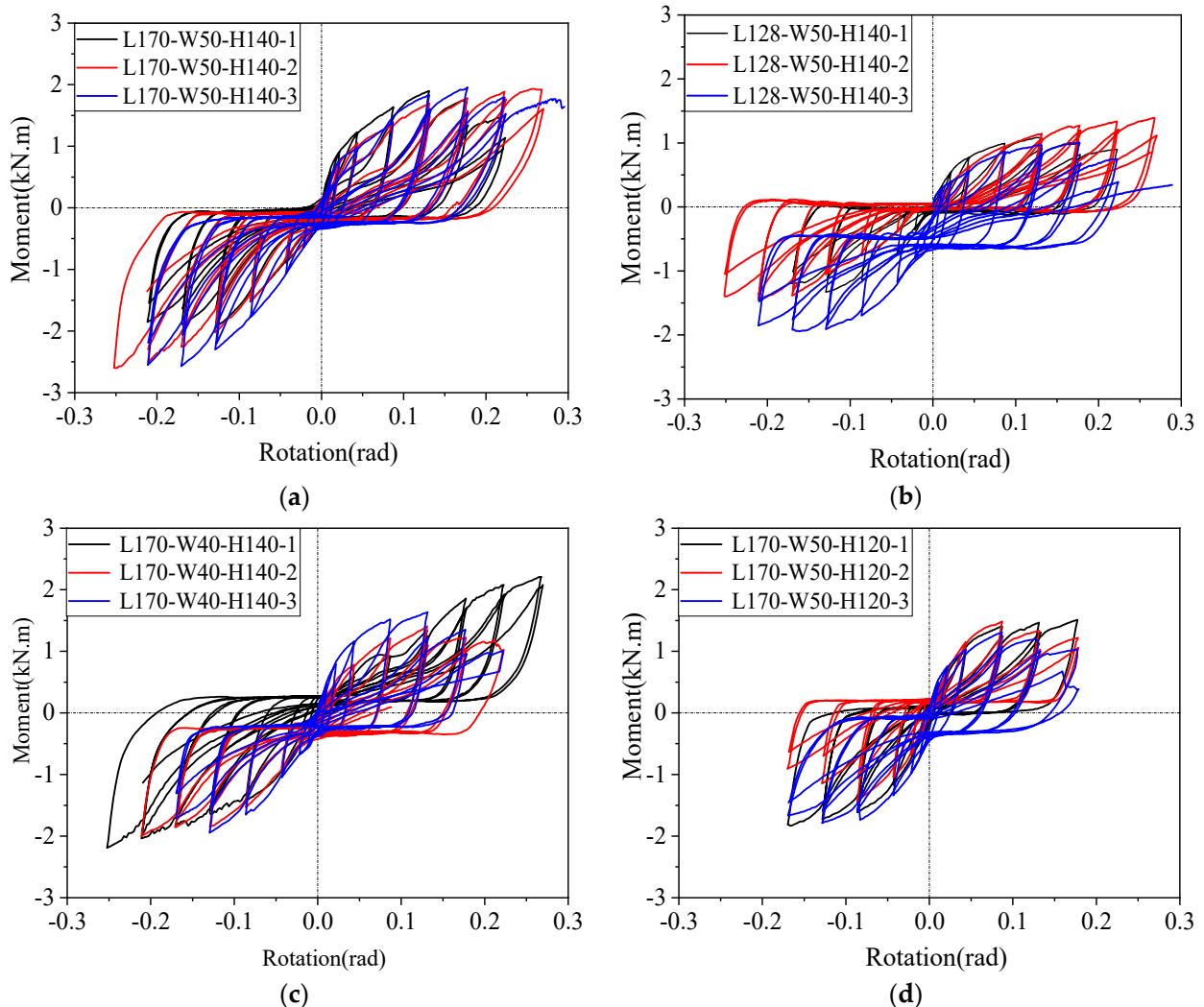


Figure 15. Hysteresis curves of the specimens. (a) Specimen L170-W50-H140, (b) Specimen L128-W50-H140, (c) Specimen L170-W40-H140, (d) Specimen L170-W50-H120.

In each group of specimens, asymmetries were observed between push and pull directions. Several hysteresis curves of specimens slightly deviate from the abscissa axis, especially for specimen L128-50-140-3, which is mainly attributed to the inherent variability of timber properties, the influence of natural timber defects, and the error during specimen fabrication.

3.5. Skeleton Curves

Figure 16 presents the moment-rotation ($M-\theta$) skeleton curves extracted from the hysteresis curves of the specimens. Among the four groups of specimens, the three skeleton curves of group L170-W50-H140 are the closest to each other, while the three skeleton curves of other groups exhibit scatter. This might be due to the material and construction defects. The average skeleton curves of each group of mortise-tenon joints are drawn in Figure 16e. It is observed that the average skeleton curves generally exhibit a clear nonlinear behavior with three stages: elastic stage, yield stage and failure stage. For all

specimens, the elastic proportion limit is around 0.02 rad. The yield stage of the curves generally ranges from 0.02 rad to 0.13 rad. The failure stage starts from 0.13 rad to the end.

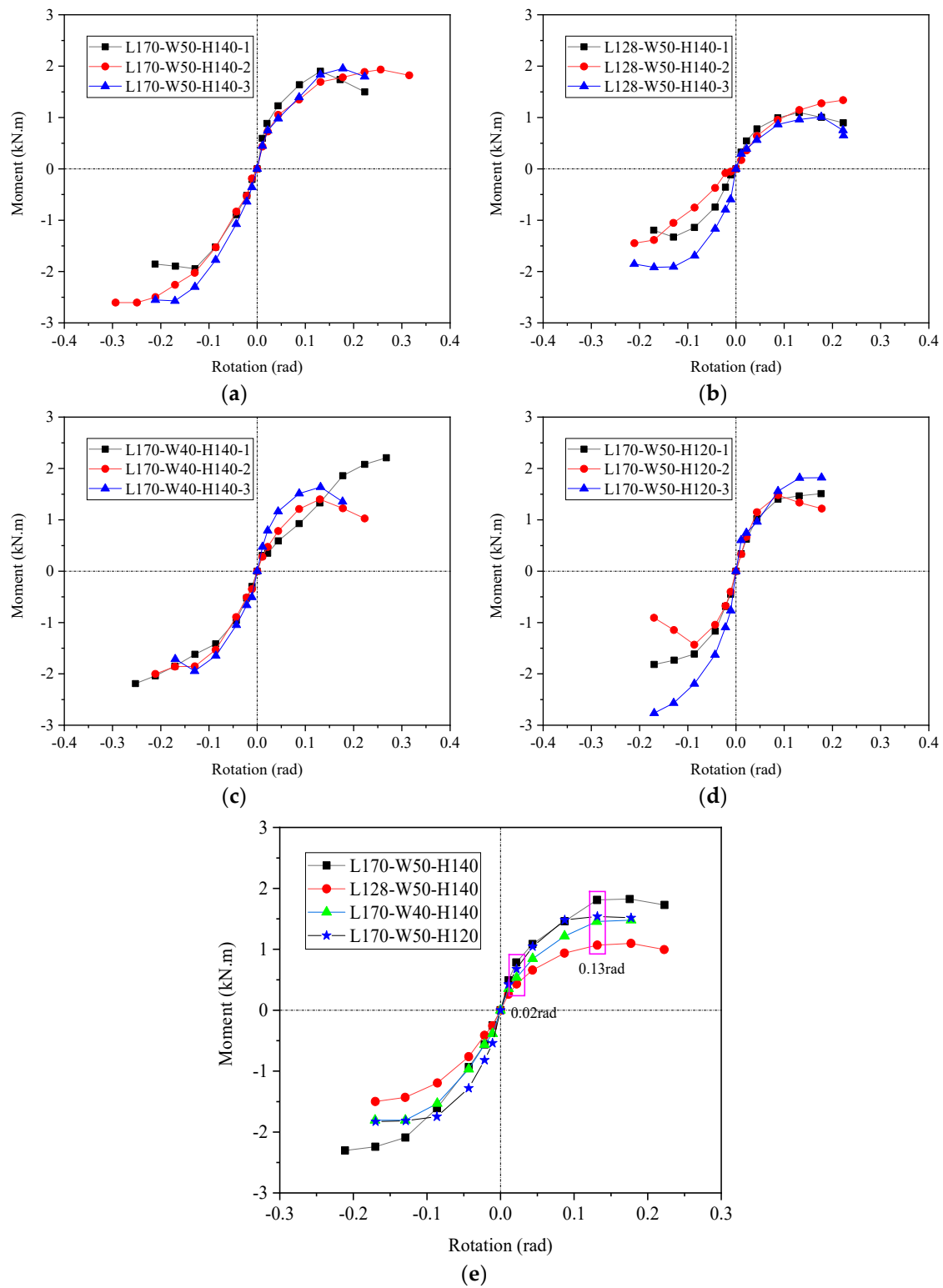


Figure 16. Skeleton curves of the specimens. (a) specimen L170-W50-H140, (b) specimen L128-W50-H140, (c) specimen L170-W40-H140, (d) specimen L170-W50-H120, (e) average skeleton curves.

3.6. Stiffness Degradation

Stiffness degradation refers to the negative correlation between the peak load and the number of cycles under the cyclic loading with constant peak displacement. K_i represents the secant stiffness of the specimen in the i th cycle of loading, which can be expressed as:

$$K_i = \frac{|+M_i| + |-M_i|}{|+\theta_i| + |-\theta_i|} \quad (2)$$

where $+M_i$ and $-M_i$ are the peak moment in the i th cycle of positive and negative loading, respectively, and $|\theta_i|$ and $|\theta_i|$ the peak rotation in the i th cycle of positive and negative loading, respectively.

The stiffness degradation of all the tested specimens is depicted in Figure 17. It is found that all the mortise-tenon joints exhibited a degradation in stiffness. The joint stiffness decreased rapidly as the rotation θ increased from 0 to 0.02 rad, and the stiffness degradation slowed once the rotation exceeded 0.05 rad. In general, the change of tenon width and height seems to have less effect on the stiffness degradation. However, the embedment length of the tenon in mortise significantly affects the stiffness degradation.

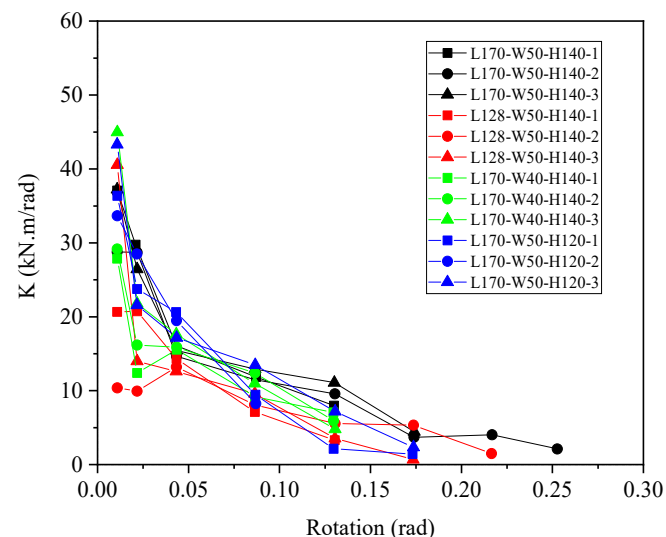


Figure 17. Stiffness degradation of the specimens.

4. Theoretical Predictions

Since it is unrealistic to perform experiments for all mortise-tenon joints to obtain the moment-rotation relationship, a theoretical model was proposed to predict the moment-rotation relationship of the joints so that the structural design of mortise-tenon joints can follow scientific and reasonable methods instead of traditional empirical methods.

4.1. Basic Assumptions

There are two extrusion regions between the mortise and tenon during the rotation of the tenon, namely, the contact area A at the bottom of the tenon and the contact area B at the top of the tenon, as shown in Figure 18. The area A of the tenon is in the middle local compression state, and the area B of the tenon is in the end local compression state. When the tenon rotates in the mortise, the extrusion stress is approximately distributed along the length of the contact areas A and B triangularly, as shown in Figure 18. Moreover, the friction-resisting tenon sliding in the contact areas was also considered. The extrusion pressure and the frictions in the two regions jointly resist the bending moment generated by the external load.

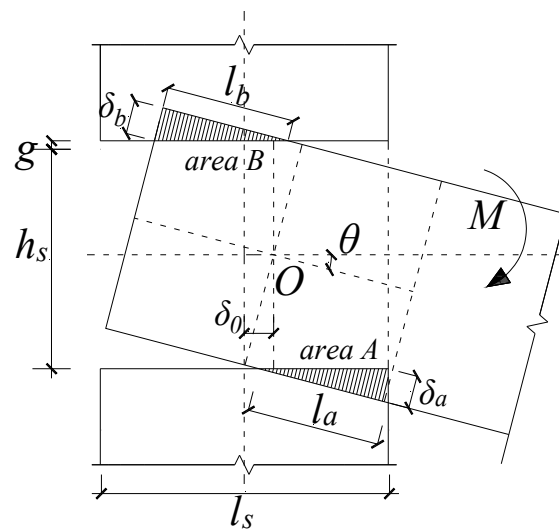


Figure 18. The deformation status of the straight mortise-tenon joint.

To predict the moment-rotation relationship, the following assumptions are made in this study:

- (1) The local extrusion deformation in the mortise was neglected. This is because the mortise is in compression parallel to the grain, so the local extrusion deformation is far less than that of the timber perpendicular to the grain.
- (2) The bi-linear local compression model proposed in this paper is used to simulate the mechanical behavior of wood in different compressive modes perpendicular to the grain.
- (3) The friction between the side surfaces of the mortise and the tenon was neglected.

4.2. Geometrical and Physical Condition

The deformation status of the straight mortise-tenon joint during rotation is shown in Figure 18. Point O is the rotation center of the tenon, and the rotation angle is represented by θ . l_a and δ_a are the extrusion length and extrusion deformation of the neck of the tenon in extrusion area A, respectively; l_b and δ_b are the extrusion length and extrusion deformation of the end of the tenon in extrusion area B, respectively. g is the initial gap between the tenon and mortise (Figure 19). The tenon's length, width, and height are indicated by l_s , b_s and h_s , respectively. b_b and b_c represent the width of the beam and column, respectively. The amount of tenon pull-out is represented by δ_0 .

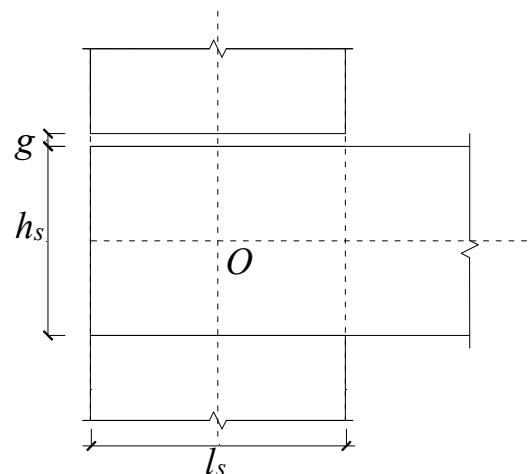


Figure 19. The initial status of the straight mortise-tenon joint.

According to geometrical conditions of the joint, δ_o , l_a , l_b and δ_a , δ_b can be expressed as:

$$\delta_o = \frac{h_s}{2} \tan \theta \quad (3)$$

$$l_a = \left(\frac{l_s}{2} - \delta_o - \frac{g}{2 \sin \theta} + \frac{h_s}{2} \tan \frac{\theta}{2} \right) / \cos \theta \quad (4)$$

$$l_b = \frac{l_s}{2} - \delta_o - \frac{g}{2 \sin \theta} \quad (5)$$

$$\delta_a = l_a \tan \theta \quad (6)$$

$$\delta_b = l_b \tan \theta \quad (7)$$

4.3. Theoretical Derivations

As shown in Figure 20, when the joint rotates, the extrusion pressures F_a and F_b and the frictions f_a and f_b were generated in extrusion area A, B respectively. The extrusion pressure is perpendicular to the tenon surface, and the friction force is opposite to the direction of the tenon sliding. The moment produced by the squeeze pressure and the friction force jointly resist the bending moment M . According to the experimental results, the theoretical mechanical model can be regarded as three stages: the sliding stage, elastic stage and plastic stage.

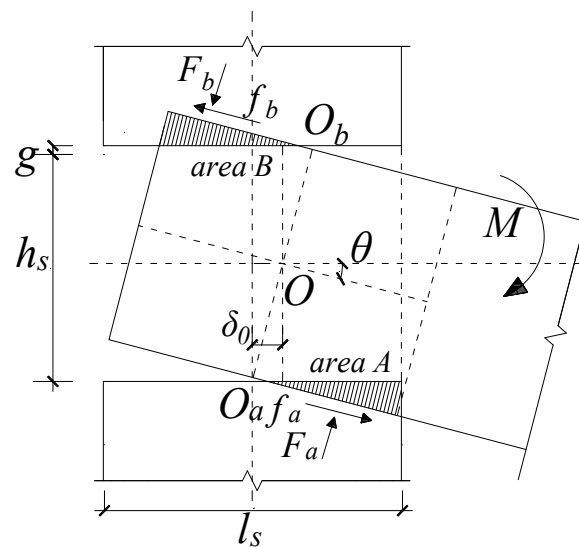


Figure 20. Stress and deformation state of the joint in rotation.

Figure 21 shows the stress state of the tenon in the contact areas A, and B in the elastic stage, the shaded area is the extrusion area between the mortise and tenon and varies with the rotation angle. δ_1 , δ_2 is the extrusion deformation at the edge of extrusion areas A and B, which can be obtained by the following equations:

$$x_0 = \frac{h_s}{2} \tan \frac{\theta}{2} + \frac{g}{2 \sin \theta} + l_a \cos^2 \theta \quad (8)$$

$$\delta_1 = \begin{cases} \delta_{1l} = \left(x - \frac{h_s}{2} \tan \frac{\theta}{2} - \frac{g}{2 \sin \theta} \right) \tan \theta & 0 < x \leq x_0 \\ \delta_{1r} = \left(\frac{h_s}{2} \tan \frac{\theta}{2} + \frac{g}{2 \sin \theta} + l_a - x \right) \cot \theta & x > x_0 \end{cases} \quad (9)$$

$$\delta_2 = \left(x - \frac{h_s}{2} \tan \frac{\theta}{2} - \frac{g}{2 \sin \theta} \right) \tan \theta \quad (10)$$

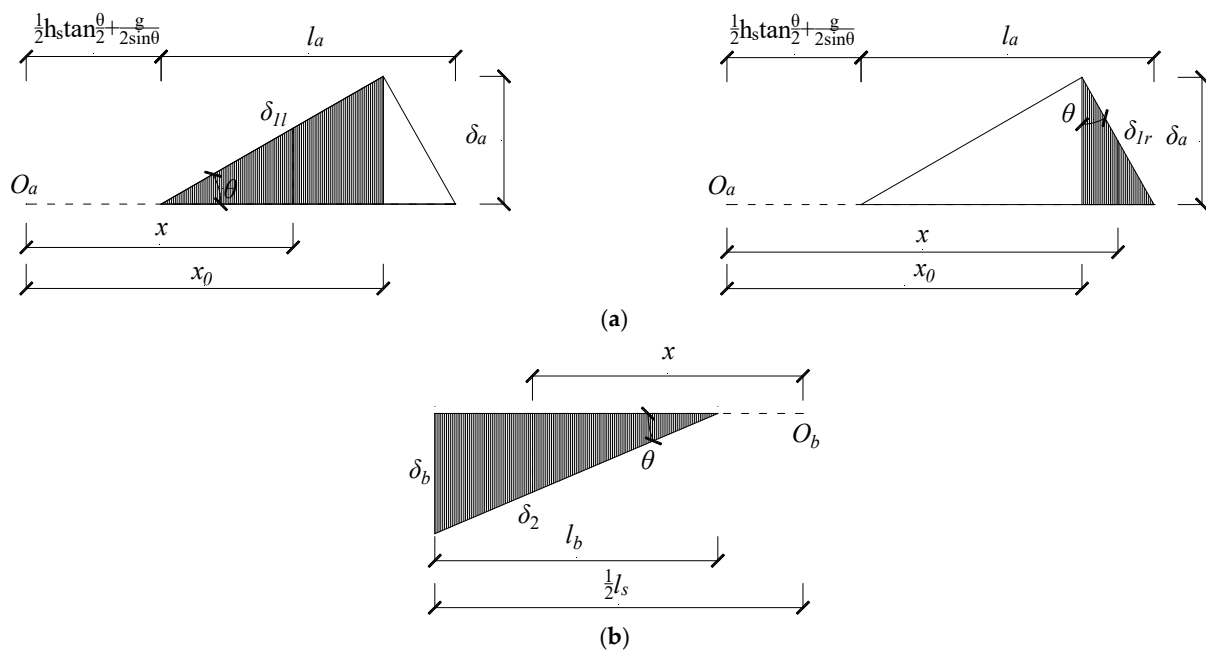


Figure 21. Stress state of the tenon in the elastic stage. (a) area “a”, (b) area “b”.

4.3.1. Sliding Stage

At the sliding stage, the tenon did not touch the mortise, the bending moment action did not exist, and the rotational deformation of the mortise was less than the initial gap. The sliding stage can be expressed by the following equation:

$$\text{When } \delta_1 < g/2 \sin \theta, \delta_2 < g/2 \sin \theta$$

$$M = 0 \quad (11)$$

4.3.2. Elastic Stage

The elastic stage starts when the rotational deformation of the tenon exceeds the initial gap and ends when the tenon emerges as plastic deformation. As shown in Figure 21a, the root of the tenon is in the middle local compression perpendicular to the grain. The force F_a and moment M_a in the pressure area A are composed of two parts, expressed in Equations (14) and (15). As shown in Figure 21b, the end of the tenon is in local end compression perpendicular to the grain. The force F_b and moment M_b in the extrusion areas are expressed in Equations (16) and (17). The equations mentioned above E_{emc} E_{eec} are elastic modulus in the middle and end local compression perpendicular to the grain, respectively, ε_{ay} and ε_{by} mean the yield strain in the middle and end local compression perpendicular to the grain.

$$\delta_{ay} = \varepsilon_{ay} h_s \quad (12)$$

$$\delta_{by} = \varepsilon_{by} h_s \quad (13)$$

$$\text{When } g/2 \sin \theta < \delta_1 < \delta_{ay}$$

$$F_a = b_s \int_{\frac{h_s}{2} \tan \frac{\theta}{2} + \frac{g}{2 \sin \theta}}^{\frac{h_s}{2} \tan \frac{\theta}{2} + l_a \cos^2 \theta} \frac{E_{emc} \delta_{1l}}{h_s} dx + b_s \int_{\frac{h_s}{2} \tan \frac{\theta}{2} + \frac{g}{2 \sin \theta}}^{\frac{h_s}{2} \tan \frac{\theta}{2} + \frac{g}{2 \sin \theta} + l_a \cos^2 \theta} \frac{E_{emc} \delta_{1r}}{h_s} dx \quad (14)$$

$$M_a = b_s \int_{\frac{h_s}{2} \tan \frac{\theta}{2} + \frac{g}{2 \sin \theta}}^{\frac{h_s}{2} \tan \frac{\theta}{2} + \frac{g}{2 \sin \theta} + l_a \cos^2 \theta} x \frac{E_{emc} \delta_{1l}}{h_s} dx + b_s \int_{\frac{h_s}{2} \tan \frac{\theta}{2} + \frac{g}{2 \sin \theta}}^{\frac{h_s}{2} \tan \frac{\theta}{2} + \frac{g}{2 \sin \theta} + l_a \cos^2 \theta} x \frac{E_{emc} \delta_{1r}}{h_s} dx \quad (15)$$

When $g/2 \sin \theta < \delta_2 < \delta_{by}$

$$F_b = b_s \int_{\frac{h_s}{2} \tan \frac{\theta}{2} + \frac{g}{2 \sin \theta}}^{\frac{l_s}{2}} \frac{E_{eec} \delta_2}{h_s} dx \quad (16)$$

$$M_b = b_s \int_{\frac{h_s}{2} \tan \frac{\theta}{2} + \frac{g}{2 \sin \theta}}^{\frac{l_s}{2}} x \frac{E_{eec} \delta_2}{h_s} dx \quad (17)$$

4.3.3. Plastic Stage

The yield strain ε_{ay} is the critical point between the elastic and plastic stages, which means the joint enters the plastic stage when the compressive strain exceeds the yield strain ε_{ay} ε_{by} . In the plastic stage, the deformation region can be divided into elastic and plastic regions, as depicted in Figure 22. The force F_a , F_b and moment M_a , M_b in the plastic stage are expressed in Equations (23)–(26). E_{pmc} and E_{pec} mean the plastic modulus in the middle and end local compression perpendicular to the grain, respectively.

$$\sigma_a = E_{emc} \varepsilon_{ay} + E_{pmc} \left(\frac{\delta_1}{h_s} - \varepsilon_{ay} \right) \quad (18)$$

$$\sigma_b = E_{eec} \varepsilon_{by} + E_{pec} \left(\frac{\delta_2}{h_s} - \varepsilon_{by} \right) \quad (19)$$

$$x_{ayl} = \frac{h_s}{2} \tan \frac{\theta}{2} + \frac{g}{2 \sin \theta} + \frac{\delta_{ay}}{\tan \theta} \quad (20)$$

$$x_{ayr} = l_a + \frac{h_s}{2} \tan \frac{\theta}{2} + \frac{g}{2 \sin \theta} - \frac{\delta_{ay}}{\cot \theta} \quad (21)$$

$$x_{by} = \frac{h_s}{2} \tan \frac{\theta}{2} + \frac{g}{2 \sin \theta} + \frac{\delta_{by}}{\tan \theta} \quad (22)$$

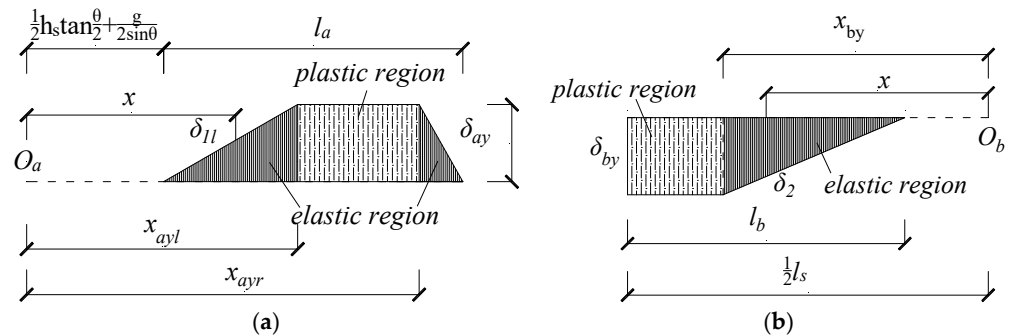


Figure 22. Stress state of the tenon in the plastic stage. (a) area “a”, (b) area “b”.

When $\delta_1 \geq \delta_{ay}$

$$F_a = b_s \int_{\frac{h_s}{2} \tan \frac{\theta}{2} + \frac{g}{2 \sin \theta}}^{x_{ayl}} \frac{E_{emc} \delta_{1l}}{h_s} dx + b_s \int_{x_{ayr}}^{\frac{h_s}{2} \tan \frac{\theta}{2} + \frac{g}{2 \sin \theta} + l_a} \frac{E_{emc} \delta_{1r}}{h_s} dx + b_s \int_{x_{ayl}}^{x_{ayr}} \sigma_a dx \quad (23)$$

$$M_a = b_s \int_{\frac{h_s}{2} \tan \frac{\theta}{2} + \frac{g}{2 \sin \theta}}^{x_{ayl}} x \frac{E_{emc} \delta_{1l}}{h_s} dx + b_s \int_{x_{ayr}}^{\frac{h_s}{2} \tan \frac{\theta}{2} + \frac{g}{2 \sin \theta} + l_a} x \frac{E_{emc} \delta_{1r}}{h_s} dx + b_s \int_{x_{ayl}}^{x_{ayr}} x \sigma_a dx \quad (24)$$

When $\delta_2 \geq \delta_{by}$

$$F_b = b_s \int_{\frac{h_s}{2} \tan \frac{\theta}{2}}^{x_{by}} \frac{E_{eec} \delta_2}{h_s} dx + b_s \int_{x_{by}}^{\frac{l_s}{2}} \sigma_b dx \quad (25)$$

$$M_b = b_s \int_{\frac{h_s}{2} \tan \frac{\theta}{2}}^{x_{by}} x \frac{E_{ecc} \delta_2}{h_s} dx + b_s \int_{x_{by}}^{\frac{h_s}{2}} x \sigma_b dx \quad (26)$$

4.3.4. M - θ Curve

The total moment of the mortise-tenon joint consists of the moment produced by the squeeze pressure and the friction force, which is expressed by Equation (29). The friction forces f_a and f_b are obtained by Equations (27) and (28), and the coefficient of friction between the tenon and mortise in this paper was taken 0.45 for Chinese fir [36]. Finally, the M - θ curve of the mortise-tenon joint can be calculated as:

$$f_a = \mu F_a \quad (27)$$

$$f_b = \mu F_b \quad (28)$$

$$M = M_a + M_b + f_a \frac{h_s}{2} + f_b \frac{h_s}{2} \quad (29)$$

4.4. Validation of Theoretical Results

According to the derived Equations (8)–(29), the theoretical M - θ curves were obtained by inputting the geometric and physical parameters of the mortise-tenon joints reported in Tables 3 and 4, specifically, the initial gap is set as 0 because there is no gap between the tenon and the mortise in this study. The comparison of the theoretical and experimental M - θ curve is shown in Figure 23.

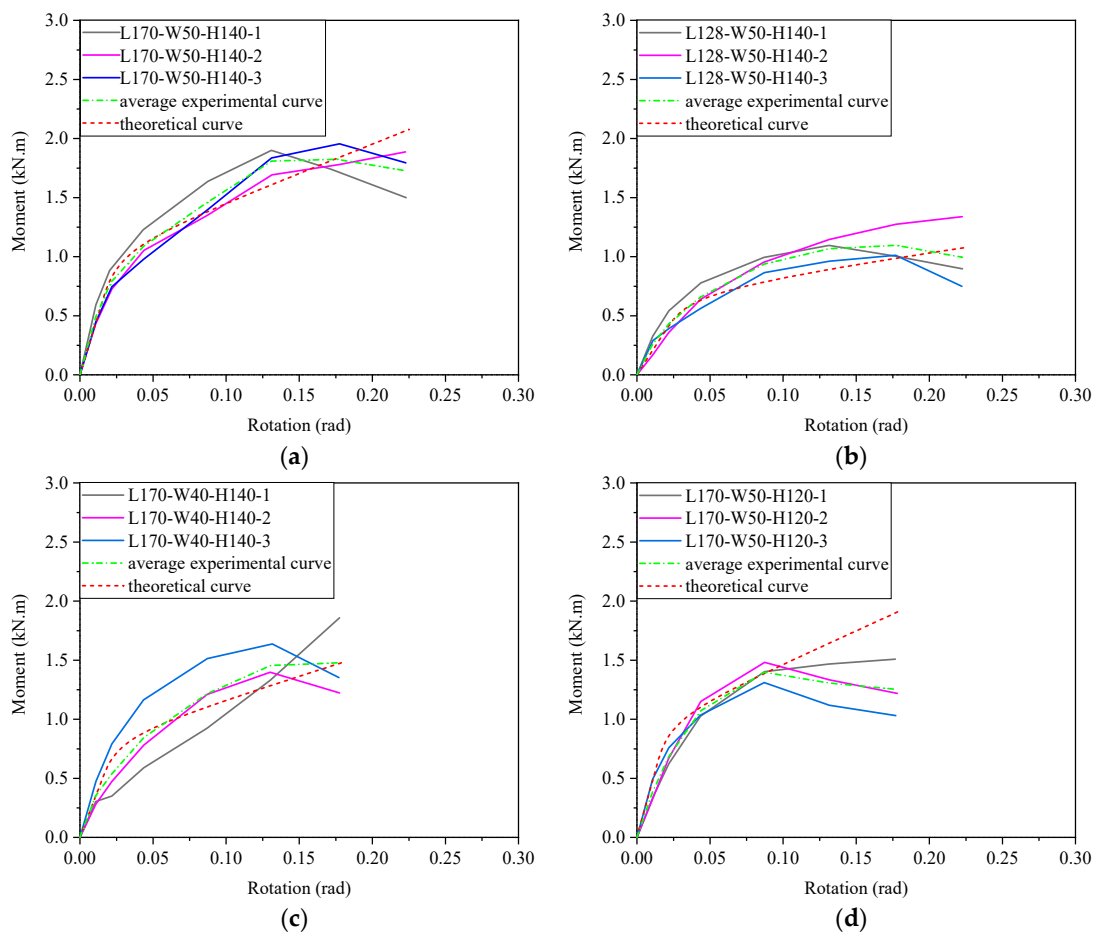


Figure 23. Comparison of the theoretical and experimental M - θ curve. (a) Specimen L170-W50-H140, (b) Specimen L128-W50-H140, (c) Specimen L170-W40-H140, (d) Specimen L170-W50-H120.

As is shown in Figure 23, the theoretical $M-\theta$ curves are generally consistent with the experimental $M-\theta$ curves. It can be observed that the yield point of the theoretical curve coincides with the yield point of the experimental $M-\theta$ curve basically, which indicates that the bi-linear model of wood compression perpendicular to grain proposed in this paper has an advantage in depicting the yield point of the $M-\theta$ curve. Among the four groups, the initial stiffness and yield moment best agree with the experimental curves of specimens L170-W50-H140, L128-W40-H140 and L170-W40-H140. The max deviation of the experimental and theoretical initial stiffness and yield moment values is 6.41% in the three groups, as shown in Table 5. In the group of L170-W50-H120, the theoretical initial stiffness and yield moment have a deviation of about 17% from the experimental values. This may be due to the difference between the theoretical and experimental pull-out amounts. The theoretical pull-out amount of the L170-W50-H120 model is smaller than the experimental pull-out amount, resulting in a higher theoretical moment and stiffness than experimental values at the same rotation.

Table 5. Comparison of the theoretical and average experimental initial stiffness and yield moment.

Specimen	M_y (kN.m)			K (kN.m/rad)		
	Avg. Exp.	Theo.	Dev.	Avg. Exp.	Theo.	Dev.
L170-W50-H140	0.78	0.83	6.41%	36.83	37.91	2.94%
L128-W50-H140	0.43	0.42	−2.33%	19.74	18.98	−3.85%
L170-W40-H140	0.63	0.66	4.76%	28.97	30.33	4.71%
L170-W50-H120	0.70	0.82	17.14%	33.33	39.00	17.01%

Note: M_y means yield moment, and K means initial stiffness.

The theoretical analysis in our previous study [37] employed an ideal elastic-plastic model for the compressive behavior of wood perpendicular to the grain, overlooking the stress-strain relationship during the plastic compression stage. In contrast, this paper employs the proposed bilinear stress-strain relationship for wood under compression perpendicular to the grain, resulting in more accurate computational analysis results. Although the proposed method can predict the mechanical behavior in the elastic and yield stage of the curves well, it needs to be improved in predicting the failure stage of the joints. Firstly, the relationship between tenon pull-out amount and rotation angle needs further study, for the decrease of the moment and stiffness of the joints is relative to the embedment length of the tenon in the mortise. The mechanical model of wood split perpendicular to grain may need to be considered because, in the failure stage, several specimens exhibited splitting and cracking failure of the tenon. In general, the theoretical model proposed is reasonable and feasible in predicting the elastic and plastic mechanical behavior of mortise-tenon joints.

5. Conclusions

This paper presents a comprehensive investigation of the moment-rotation relationship of straight mortise-tenon joints, including local compression tests perpendicular to the grain in three different compressive modes and cyclic loading tests of four groups of joints. Finally, a theoretical moment-rotation model was proposed to predict the mechanical behavior of the mortise-tenon joints. The main results are summarized as follows.

- (1) The results of the compression tests perpendicular to grain indicated that the yield stress, elastic modulus, and plastic modulus in local compression perpendicular to grain are greater than that in the end local compression and full compression perpendicular to grain. A most approximate area method was used to estimate the yield point of the strain-stress curve, which is good at estimating the theoretical yield point.
- (2) The cyclic loading tests showed that the mortise-tenon joints mainly failed by tenon pull-out, crush in local compression, splitting perpendicular to grain and breakage of the tenon. The hysteresis curves of the tested specimens generally exhibit a “Z” shape,

which indicates a typical pinching effect. As a result, the moment and initial rotation stiffness of the joint both decrease with the reduction of the tenon length (L), width (W), and height (H). The parameter tenon length and width have a more significant influence on the mechanical behavior of the joints because the mechanical behavior is mainly determined by the compression area formed with tenon length and width.

- (3) A theoretical model based on physical and geometric parameters of the mortise-tenon joints was proposed to predict the mechanical behavior, considering middle local compression in the neck of the tenon and end local compression at the end of the tenon. By comparing the theoretical $M-\theta$ curves with the experimental $M-\theta$ curves, it was found that the theoretical model proposed is reasonable and feasible in predicting the elastic and plastic mechanical behavior of mortise-tenon joints but needs to be improved in predicting the failure mechanical behavior.

Author Contributions: Conceptualization, W.L. and X.L.; methodology, W.L. and X.L.; formal analysis, F.X. and K.Y.; investigation, X.L. and K.L.; data curation, K.L.; writing—original draft preparation, X.L. and Z.L.; writing—review and editing, K.Y. and Z.L.; funding acquisition, W.L. All authors have read and agreed to the published version of the manuscript.

Funding: This research was funded by the National Natural Science Foundation of China, grant number 51678298.

Data Availability Statement: The data in this paper are given in the tables and figures within the manuscript.

Conflicts of Interest: The authors declare no conflict of interest.

References

- Liang, S. *Construction Technology of Chinese Ancient Timber Structures*; Tsinghua University Press: Beijing, China, 2007.
- Ma, B. *Construction Technology of Chinese Ancient Timber Structures*; Science Press: Beijing, China, 2003.
- Chang, W.; Hsu, M.F.; Komatsu, K. Rotational performance of traditional Nuki joints with gap I: Theory and verification. *J. Wood Sci.* **2006**, *52*, 58–62. [[CrossRef](#)]
- Yue, Z. Traditional Chinese wood structure joints with an experiment considering regional differences. *Int. J. Arch. Herit.* **2014**, *8*, 224–246. [[CrossRef](#)]
- Feio, A.; Lourenço, P.; Machado, J. Testing and modeling of a traditional timber mortise and tenon joint. *Mater. Struct.* **2014**, *47*, 213–225. [[CrossRef](#)]
- Xie, Q.; Zhang, L.; Li, S.; Zhou, W.; Wang, L. Cyclic behavior of Chinese ancient wooden frame with mortise-tenon joints: Friction constitutive model and finite element modelling. *J. Wood Sci.* **2018**, *64*, 40–51. [[CrossRef](#)]
- Xie, Q.; Zhang, L.; Wang, L.; Zhou, W.; Zhou, T. Lateral performance of traditional Chinese timber frames: Experiments and analytical model. *Eng. Struct.* **2019**, *186*, 446–455. [[CrossRef](#)]
- Xie, Q.; Wang, L.; Zheng, P.; Zhang, L.; Hu, W. Rotational behavior of degraded traditional mortise-tenon joints: Experimental tests and hysteretic model. *Int. J. Archit. Herit.* **2018**, *12*, 125–136. [[CrossRef](#)]
- Guan, Z.; Kitamori, A.; Komatsu, K. Experimental study and finite element modelling of Japanese “Nuki” joints: Part one: Elastic stress states subjected to different wedge configurations. *Eng. Struct.* **2008**, *30*, 2032–2040. [[CrossRef](#)]
- Guan, Z.; Kitamori, A.; Komatsu, K. Experimental study and finite element modelling of Japanese “Nuki” joints: Part two: Racking resistance subjected to different wedge configurations. *Eng. Struct.* **2008**, *30*, 2032–2040. [[CrossRef](#)]
- Xu, M. Study of Aseismic Behavior of Mortise-Tenon Joints in Chinese Ancient Timber Buildings. Ph.D. Thesis, Southeast University, Nanjing, China, 2011.
- Chen, L.K.; Li, S.C.; Zhao, K.P.; Chen, Z.Y.; Song, T.; Zhang, L.; Jang, Z.J. Experimental and numerical investigation on seismic performance of one-way straight mortise-tenon joints based on a novel method to simulate damage of deteriorated ancient Chinese timber buildings. *J. Perform. Constr. Facil.* **2020**, *34*, 04019119. [[CrossRef](#)]
- Panoutsopoulou, L.; Mouzakis, C. Experimental investigation of the behavior of traditional timber mortise-tenon T-joints under monotonic and cyclic loading. *Constr. Build. Mater.* **2022**, *348*, 128655. [[CrossRef](#)]
- Keita, O.; Yasutoshi, S.; Mariko, Y. Theoretical estimation of the mechanical performance of traditional mortise-tenon joint involving a gap. *J. Wood Sci.* **2016**, *62*, 242–250.
- Yang, Q.; Pan, Y.; Law, S. Load resisting mechanism of the mortise-tenon connection with gaps under in-plane forces and bending moments. *Eng. Struct.* **2020**, *219*, 110755. [[CrossRef](#)]
- Yang, Q.; Gao, C.; Wang, J.; Ren, K.; Yang, N. Probability distribution of gaps between tenon and mortise of traditional timber structures. *Eur. J. Wood Wood Prod.* **2020**, *78*, 27–39. [[CrossRef](#)]

17. Ma, L.; Xue, J.; Dai, W.; Zhang, X.; Zhao, X. Bending moment-rotation relationship of mortise-tenon connections in historic timber structures. *Constr. Build. Mater.* **2020**, *232*, 117285. [[CrossRef](#)]
18. Zhang, B.; Xie, Q.; Li, S.; Zhang, L.; Wu, Y. Effects of gaps on the rotational performance of traditional straight mortise-tenon joints. *Eng. Struct.* **2022**, *260*, 114231. [[CrossRef](#)]
19. He, J.; Yu, P.; Wang, J.; Yang, Q.; Han, M.; Xie, L. Theoretical model of bending moment for the penetrated mortise-tenon joint involving gaps in traditional timber structure. *J. Build. Eng.* **2021**, *42*, 103102. [[CrossRef](#)]
20. Inayama, M. Embedment Theory of Timber and Its Application. Ph.D. Thesis, The University of Tokyo, Tokyo, Japan, 1991.
21. Leijten, A. A general bearing deformation model for timber Compression perpendicular to grain. *Constr. Build. Mater.* **2018**, *165*, 707–716. [[CrossRef](#)]
22. Leijten, A.; Jorissen, A.; De Leijer, B. The local bearing capacity perpendicular to grain of structural timber elements. *Constr. Build. Mater.* **2012**, *27*, 54–59. [[CrossRef](#)]
23. Moseng, M.; Hagle, D. *The Capacity of Wood for Compression Perpendicular to the Grain*; Institute for Matematiske Realfag og Teknologi NMBU: Oslo, Norway, 2012.
24. *GB/T 1927.13-2022*; Test Methods for Physical and Mechanical Properties of Small Clear Wood Specimens—Part 13: Determination of the Modulus of Elastic in Compression Perpendicular to Grain. Standardization Administration of China Press: Beijing, China, 2022.
25. *GB/T 1927.11-2022*; Test Methods for Physical and Mechanical Properties of Small Clear Wood Specimens—Part 11: Determination of Ultimate Stress in Compression Parallel to Grain. Standardization Administration of China Press: Beijing, China, 2022.
26. *GB/T 1927.14-2022*; Test Methods for Physical and Mechanical Properties of Small Clear Wood Specimens—Part 14: Determination of Tensile Strength Parallel to Grain. Standardization Administration of China Press: Beijing, China, 2022.
27. *GB/T 1927.16-2022*; Test Methods for Physical and Mechanical Properties of Small Clear Wood Specimens—Part 16: Methods of Testing in Shearing Strength Parallel to Grain of Wood. Standardization Administration of China Press: Beijing, China, 2022.
28. *B/T 50329-2012*; Standard for Test Methods of Timber Structures. Standardization Administration of China Press: Beijing, China, 2012.
29. Li, S.; Zhou, Z.; Luo, H.; Milani, G. Behavior of traditional Chinese mortise-tenon joints: Experimental and numerical insight for coupled vertical and reversed horizontal loads. *J. Build. Eng.* **2020**, *30*, 101257. [[CrossRef](#)]
30. Ling, Z.; Xiang, Z.; Liu, W.; Yang, H.; Tang, J. Load-slip behaviour of glue laminated timber connections with glued-in steel rod parallel to grain. *Constr. Build. Mater.* **2019**, *227*, 117028. [[CrossRef](#)]
31. Ling, Z.; Zhang, H.; Mu, Q.; Xiang, Z.; Zhang, L.; Zheng, W. Shear performance of assembled shear connectors for timber–concrete composite beams. *Constr. Build. Mater.* **2022**, *329*, 127158. [[CrossRef](#)]
32. Feng, P.; Cheng, S.; Bai, Y.; Ye, L. Mechanical behavior of concrete-filled square steel tube with FRP-confined concrete core subjected to axial compression. *Compos. Struct.* **2015**, *123*, 312–324. [[CrossRef](#)]
33. *ISO 13061-5*; Physical and Mechanical Properties of Wood—Test Methods for Small Clear Wood Specimens—Part 5: Determination of Strength in Compression Perpendicular to Grain. International Organization for Standardization: Geneva, Switzerland, 2020.
34. *BS EN 408*; Timber Structures—Structural Timber and Glued Laminated Timber—Determination of Some Physical and Mechanical Propertie. British Standards Institution: London, UK, 2010.
35. *JGJ 159-2008*; Code for Construction and Acceptance of Ancient Chinese Architecture Engineering. China Architecture and Building Press: Beijing, China, 2008.
36. Liu, K. Experimental Study on Mechanical Characteristics of Mortise and Tenon Joints Considering the Local Compression. Master’s Thesis, Nanjing Tech University, Nanjing, China, 2016.
37. Lu, W.; Xu, F.; Liu, K.; Zhang, K.; Liu, X.; Liu, W. Mechanical properties of mortise-tenon joints considering local compression effect. *J. Build. Struct.* **2019**, *40*, 37–44. (In Chinese)

Disclaimer/Publisher’s Note: The statements, opinions and data contained in all publications are solely those of the individual author(s) and contributor(s) and not of MDPI and/or the editor(s). MDPI and/or the editor(s) disclaim responsibility for any injury to people or property resulting from any ideas, methods, instructions or products referred to in the content.